Published in partnership with CECCR at King Abdulaziz University



https://doi.org/10.1038/s41612-025-01221-7

Distinct Hadley circulation attributable to rapid and slow El Niño decay and its regional impacts

Check for updates

Xuanliang Ji^{1,2,3,4}, Juan Feng^{1,2}, Jianping Li^{5,6} & Yazhou Zhang^{5,6}

El Niño significantly impacts the global Hadley circulation (HC), however, the modulation of different decay rates of El Niño on the HC is overlooked. Our research reveals that rapid decay (RD) events cause the global HC to exhibit an equatorially asymmetric configuration, in contrast to the quasi-symmetric structure seen during slow decay (SD) events. This is primarily driven by HC anomalies in the central-eastern Pacific, influenced by anomalous sea surface temperatures that impact the conversion of atmospheric perturbation potential energy to kinetic energy. The structure of regional HC anomalies in the Indo-Pacific Warm Pool (IPWP) exhibits contrasting patterns within different events. During RD (SD) events, the intensified (weakened) regional HC over the IPWP results in increased (decreased) terrestrial precipitation over its coastal countries. Therefore, our findings have important implications for understanding and predicting regional climate impacts associated with different El Niño decay patterns.

El Niño is a naturally occurring phenomenon characterized by fluctuations in sea surface temperature anomalies (SSTA) over the central-eastern Pacific (CEP) region, renowned for its significant interannual variability^{1,2}. These fluctuations exhibit diverse amplitudes, temporal progressions, and spatial configurations^{3–7}, consequently exerting essential impacts on global climate^{8–10}. The variable duration of El Niño events has sparked significant interest in understanding its decay characteristics within the climate research community^{11,12}.

Notably, about 40% of El Niño events from 1950 to 2020 exhibit slow decay (SD) characteristics ¹², challenging the conventional view that El Niño typically ends rapidly after its winter peak. Moreover, different decay rates of El Niño events manifest distinct climate effects. Rapid decay (RD) events result in a swift shift to negative SSTA in the CEP region, giving rise to a stronger, more frequent, and broader anomalous anticyclone (AAC) over the northwest Pacific (NWP). In contrast, SD events, characterized by persistent positive SSTA in the same region, exert a weaker influence on the AAC^{13–15}. The differing decay rates cause shifts in the position of the AAC, leading to diverse rainfall anomalies in East Asia. RD events are associated with positive rainfall anomalies throughout eastern China, while SD events concentrate positive anomalies in the Yangtze-Huaihe River basin¹⁶. Moreover, the SSTA in the tropical Indian Ocean (IO) and its impact on

summer precipitation in South Asia during El Niño decay years are closely linked to the El Niño decay rate^{17–19}. Future projections show prolonged eastern Pacific warm SSTA following El Niño peaks. Their persistence into the boreal spring shifts tropical Pacific convection eastward, modifies the Pacific-North American teleconnection, and drives a northeastward shift of temperature and precipitation anomalies over North America²⁰. Additionally, northern tropical Atlantic warming in the boreal spring of El Niño decaying years is stronger and more persistent during SD than RD events¹¹. Consequently, different patterns of SSTA, particularly in the tropical IO and the tropical Pacific Ocean, emerge under varying El Niño decay rates. Although previous studies have focused primarily on the regional climate impacts and teleconnection patterns associated with these varying decay rates, the extent to which they influence the global-scale circulation system remains uncertain.

The Hadley circulation (HC) is a thermodynamic system characterized by two closed cells: the upward branch corresponding to the intertropical convergence zone and the downward branches associated with the subtropical high-pressure belts in each hemisphere. Through its vertical overturning and horizontal transport, the HC exports tropical water vapor and energy to subtropical and extratropical regions while returning moisture equatorward near the surface, thereby exerting primary control over global

¹State Key Laboratory of Remote Sensing Science, Faculty of Geographical Science, Beijing Normal University, Beijing, China. ²Beijing Engineering Research Center for Global Land Remote Sensing Products, Faculty of Geographical Science, Beijing Normal University, Beijing, China. ³State Key Laboratory of Satellite Ocean Environment Dynamics, National Marine Environmental Forecasting Center, Beijing, China. ⁴Key Laboratory of Research on Marine Hazards Forecasting, Ministry of Natural Resources, Beijing, China. ⁵Frontiers Science Center for Deep Ocean Multi-spheres and Earth System/Key Laboratory of Physical Oceanography/Academy of the Future Ocean, Ocean University of China, Qingdao, China. ⁵Laoshan Laboratory, Qingdao, China. ⊡e-mail: fengjuan@bnu.edu.cn

temperature, precipitation patterns, drought occurrence, and large-scale weather systems^{21–24}. El Niño substantially modifies the HC's strength^{25,26}, width^{27,28}, and variability^{24,29,30} of the HC, chiefly by altering the spatial pattern of SSTA. However, most studies have emphasized global HC responses to El Niño phase (e.g., development, maturity, decay)^{27,31,32}; the influence of varying El Niño decay rates—particularly on regional HC anomalies—remains inadequately explored.

Numerous studies underscore the pivotal role of regional HC intensity and the latitude of its poleward edge in driving climate variability^{8,24,33,34} Variations in regional HC substantially modulate tropical cyclone activity over the Atlantic and western Pacific²⁴, and alter precipitation regimes in Australia and Asia³⁵ as well as in South America³⁶. Regional HC anomalies have also been implicated in observed declines in precipitation over West Africa and northern China, and in changes in snow accumulation across the southern Himalaya, although substantial uncertainties remain regarding the magnitude and mechanisms of these links^{37,38}. Recent work has advanced our understanding of interannual variability in regional HC dynamics and clarified some of their climatic impacts^{8,39}. Nonetheless, previous studies have not yet explored the linkage between the HC and varying El Niño decay rates. Whether different El Niño decay types exert distinct influences on the global and regional HC, and the extent to which regional HC anomalies contribute to changes in the global HC and its associated climate impacts, remain unresolved and warrant further investigation. In this study, we utilize multiple reanalysis datasets and models within an atmospheric energetics framework to demonstrate that the global annual-mean HC exhibits anomalous equatorial asymmetrical (quasi-symmetrical) structures during RD (SD) events. This configuration is primarily modulated by regional HC dynamics within the CEP region. Furthermore, the intensity of regional HC in the Indo-Pacific warm Pool (IPWP) region enhances during RD events but suppresses during SD events, leading to contrasting impacts on precipitation patterns across *South Asia*, *China*, *Australia*, and the *Maritime Continent*.

Results

Distinct meridional gradient of underlying SSTA within the RD and SD events

Firstly, we classified the 25 El Niño events spanning from 1950 to 2022 into 14 RD and 11 SD events (RD and SD events, Methods). El Niño typically peaks in boreal winter, followed by a transition to La Niña by the next summer (Supplementary Fig. 1b, red). However, RD and SD events deviate significantly: RD events (blue) exhibit a higher peak and rapid cooling to negative SSTA by the following April-May-June (AMJ), while SD events (yellow) feature a lower peak but sustained positive anomalies through autumn. Though their development is synchronous, RD events reverse phase by the following AMJ, in contrast to SD events, which maintain a positive Niño-3.4 index throughout the entire year post-peak. Additionally, distinctive anomalous spatial patterns emerge in the SSTA across these events, particularly evident in the tropical Pacific warm pool and the CEP regions. The SSTA in the Pacific mirrors that of a La Niña pattern⁴⁰ during RD events, characterized by significant negative anomalies throughout the CEP (Fig. 1a, shading), accompanied with two anomalous anticyclonic systems on either side of the equator (Fig. 1a, contour line). The anticyclone in the Northern Hemisphere (NH) is associated with anomalous easterlies in the NWP region, enhancing the intensity of the trade winds, while the Southern Hemisphere (SH) anticyclone features westerlies that reduce the climatological wind there. Based on the wind-evaporation-SST feedback mechanism⁴¹, substantial cold SSTA are detected in the region north of the equator in the tropical Pacific, whereas warm SSTA south of the equator.

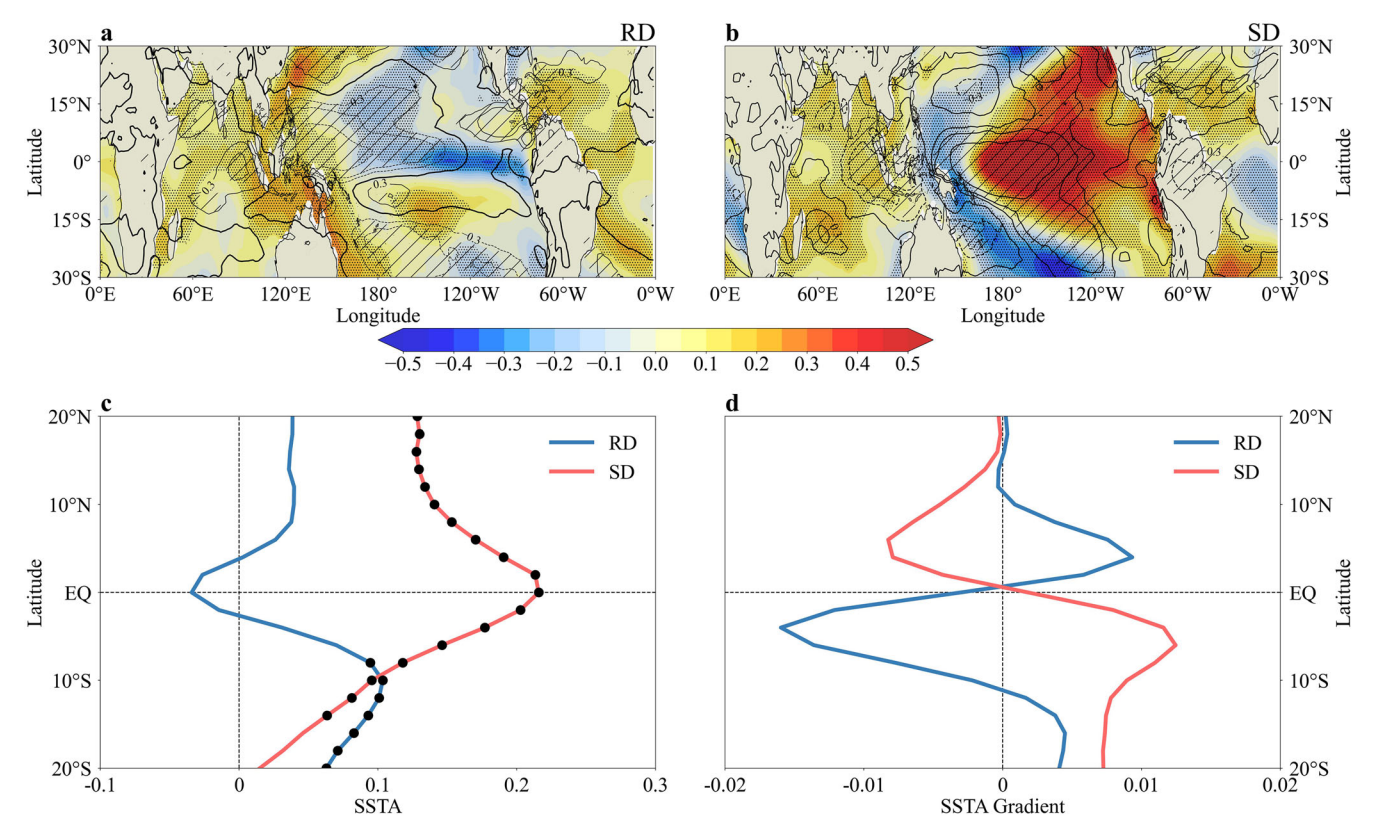


Fig. 1 | Spatial distributions of Sea Surface Temperature Anomalies (SSTA) and zonal wind anomalies during the rapid decaying (RD) and slow decaying (SD) El Niño decay events. Composite differences of annual mean SSTA (shading, units: °C) based on Extended Reconstructed Sea Surface Temperature v5 (ERRSTV5) and zonal wind anomalies (contour line, units: m·s⁻¹) based on European Centre for Medium-Range Weather Forecasts (ECMWF) Reanalysis v5 (ERA5) during the RD

(a) and SD (b) events. c, d Meridional distribution of global zonal-mean annual mean SSTA (c; units: °C) and its gradients using central differential (d; units: $10^{-5} \cdot ^{\circ} \text{C} \cdot \text{m}^{-1}$) during the RD and SD events, respectively. In a-c, the slash areas and dark spots indicate statistically significant anomalies of zonal wind, SST, and zonal-mean SSTA at the 0.05 level based on the two-sided Student's *t* test, respectively.

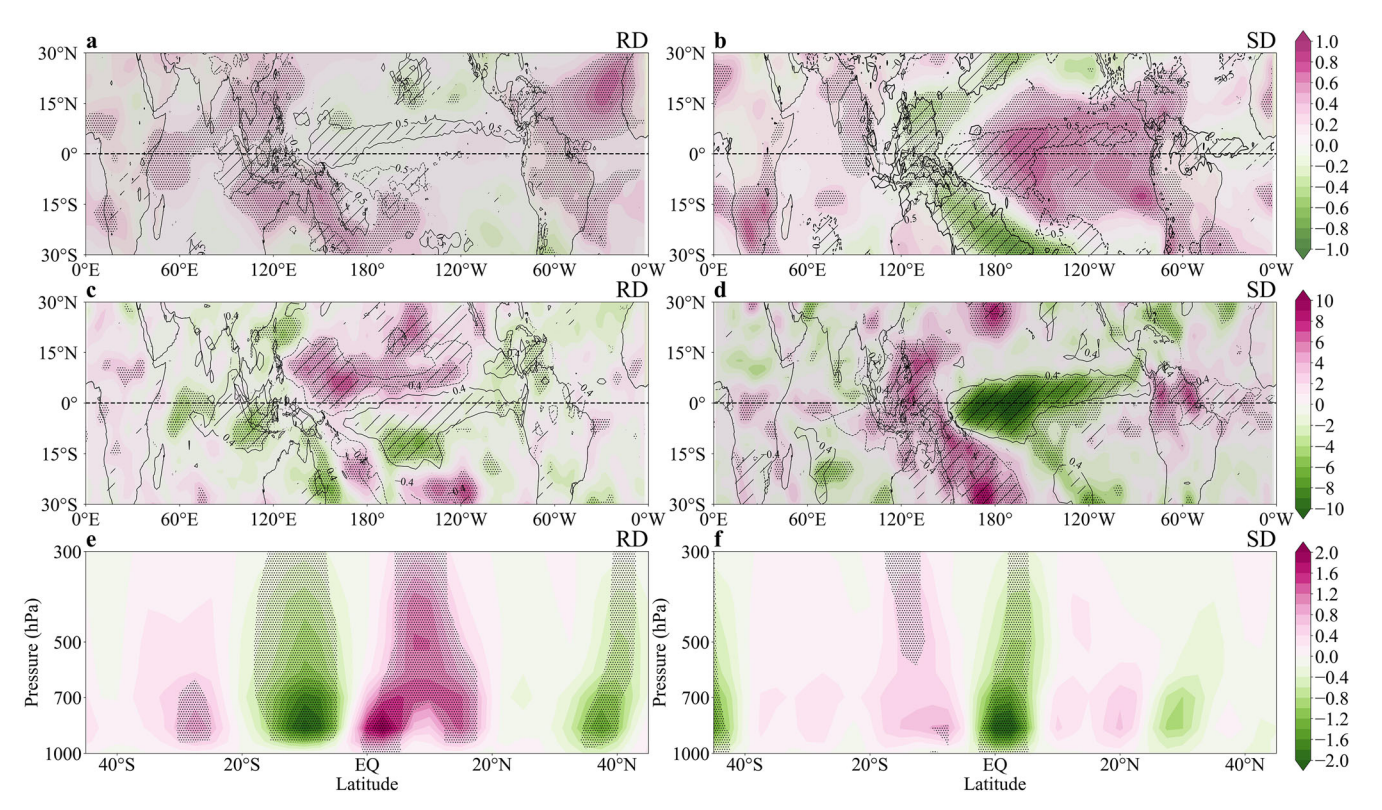


Fig. 2 | Anomalous distributions of the perturbation potential energy (*PPE*), energy conversion term (C_k), vertical velocity and precipitation during the RD and SD events. Composite differences of annual mean *PPE* anomalies (shading, units: 10^6 ·J·m⁻²) and pressure velocity anomalies (contour line, units: 10^{-2} ·Pa·s⁻¹) at 850 hPa based on ERA5 dataset from 1950 to 2022 during the RD (**a**) and SD (**b**) events. **c**, **d** same as in (**a**, **b**), but for the anomalies of annual mean C_k (shading, units: W·m⁻²) based on ERA5 dataset from 1950 to 2022 and annual mean precipitation

(contour line, units: mm·d⁻¹) based on Global Precipitation Climatology Project (GPCP) dataset from 1979 to 2022. Vertical distribution of global zonal-mean C_k during the RD (**e**) and SD (**f**) events. In (**a**-**d**), the dark spots indicate statistically significant of *PPE* and C_k at the 0.05 level using Student's two-sided t-test, and slashes indicate statistically significant of vertical velocity and precipitation at the 0.05 level based on the two-sided Student's t test. In **e**, **f** the dark spots indicate statistically significant anomalies of C_k at the 0.05 level based on the two-sided Student's t test.

Additionally, the anomalous easterlies over the equatorial Pacific would induce the upwelling Kelvin waves that propagate eastward^{42,43}, progressively attenuating warming in the eastern Pacific. This process is further linked to a shallower thermocline in the eastern Pacific, resulting in significant negative SSTA through thermocline feedback mechanism⁴. Simultaneously, a westward shift and intensification of the Walker circulation (WC, Walker Circulation, METHODS) has been detected (Supplementary Fig. 2), favoring warm SSTA in the western Pacific. Significant positive SSTA are also noted in the IO and tropical Atlantic, consistent with previous findings^{16,19}. However, the IO SSTA exhibits an east-west seesaw pattern, with greater amplitude in the eastern. Consequently, elevated temperatures correspond to the upward branch of the WC within the warm pool. In conjunction, the global zonal-mean SSTA exhibits an asymmetric structure during RD events, with the peak positive anomalies located near 10°S (Fig. 1c).

In contrast, during SD events, the spatial distribution of SSTA is similar to El Niño pattern, with positive SSTA in the central-eastern equatorial Pacific and negative SSTA in the west (Fig. 1b, shading). This pattern arises primarily from the sustained influence of westerly wind anomalies over the Pacific (Fig. 1b, contour line). Meanwhile, positive SSTA continue to be observed in the IO but with a different zonal distribution. The IO SSTA exhibit higher values in the western region, with elevated temperatures situated near 70°E, aligning with the anomalous WC upward branch (Supplementary Fig. 2). The initiation of zonal winds in the RD and SD stages may be influenced by the intensity and distribution of IO SSTA¹⁹. When the IO is dominated by positive SSTA¹⁵ or stronger negative SSTA in the western IO¹⁹, conditions become favorable for forming anomalous easterlies in the western and central equatorial Pacific during the summer of decay years, potentially accelerating the decline of El Niño. Conversely, it

would slow down the rate of decay⁴⁴. Additionally, the SSTA in the South Atlantic transition from positive during RD events to negative during SD events, aligning with prevailing westerlies and easterlies anomalies, respectively. Consequently, the meridional distribution of global zonal-mean SSTA becomes equatorially symmetrical during SD events (Fig. 1c). Correspondingly, the evolution of longitudinal-mean distribution of global SSTA (Supplementary Fig. 3) corroborates distinct meridional characteristics, showing equatorial asymmetric feature with greater amplitude to the south of the equator during RD events, and equatorial symmetric feature during SD events.

Contrasting SSTA patterns in RD and SD El Niño events imply differing latent heat release and diabatic heating processes, and thus energy conversion pathways. Diabatic heating process facilitates the conversion of potential energy into kinetic energy⁴⁵, thereby influencing the formation and persistence of atmospheric circulation patterns. Furthermore, atmospheric perturbation potential energy (PPE) reflects the energy conversion resulting from the interaction between the atmosphere and ocean⁴⁶. Thus, we conduct further analysis to quantify the PPE (Atmospheric Perturbation Potential Energy, Methods). During RD and SD events, distinct spatial patterns of anomalous PPE are evident, showing strong coherence with the associated SSTA (Fig. 1a, b). As defined by Eq. 10 (Atmospheric Perturbation Potential Energy, Methods), diabatic heating serves as the direct source term for PPE. Thus, a positive diabatic heating anomaly generates PPE, while a negative anomaly indicates its consumption. Consistent with this, RD events exhibit notable positive atmospheric PPE anomalies over the equatorial Western Pacific Warm Pool (WPWP) region (Fig. 2a). Conversely, SD events display persistent positive PPE anomalies predominantly in the CEP region along the equator (Fig. 2b). These distinct patterns underscore that atmospheric

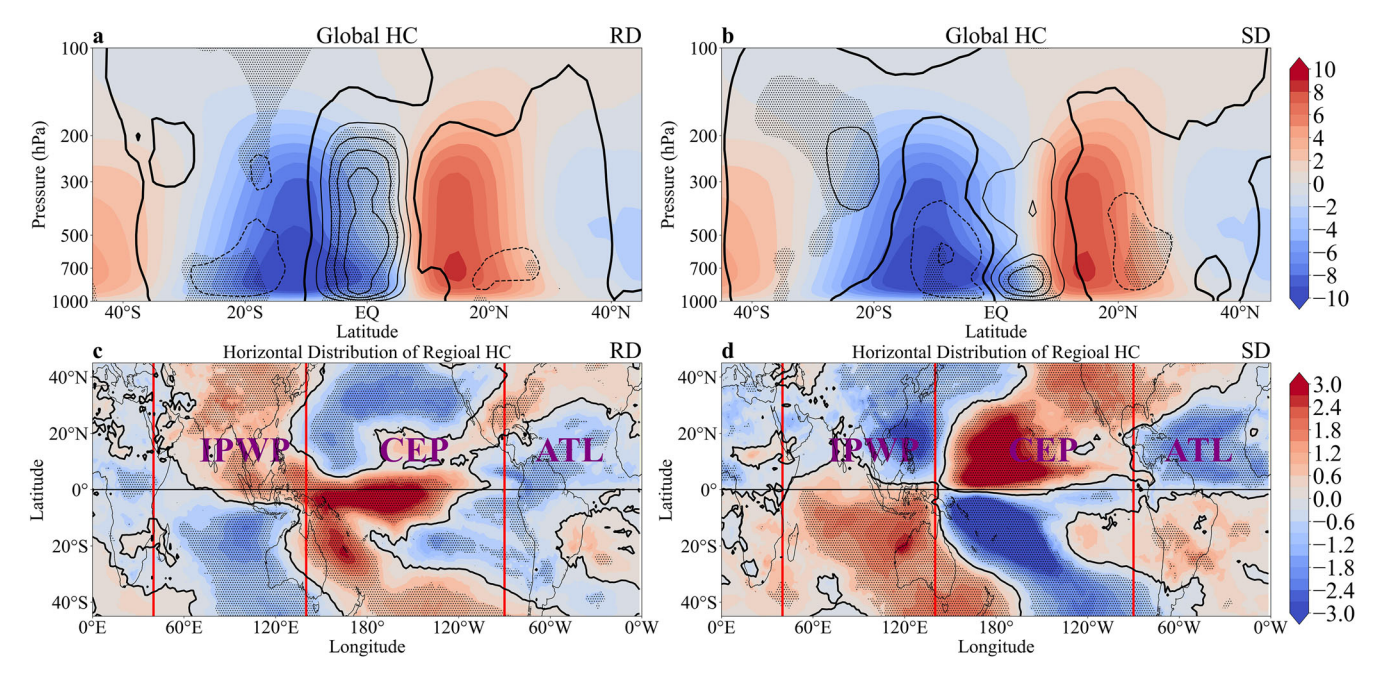


Fig. 3 | Vertical and horizontal distribution of mass stream function (MSF) anomalies based on ERA5 dataset during the RD and SD events from 1950 to 2022. Composite differences of annual mean MSF anomalies (contour line, with an interval of $0.15 \times 10^{10} \, \text{kg·s}^{-1}$) and its climatological mean (shading, with an interval of $2 \times 10^{10} \, \text{kg·s}^{-1}$) during RD (a) and SD (b) events, respectively. c, d Horizontal distribution of the regional annual mean MSF anomalies (shading, with an interval of $0.6 \times 10^{10} \, \text{kg·s}^{-1}$) during RD (c) and SD (d) events, respectively. The

regional MSF is defined as the maximum strength along the vertical level of the HC at each grid point. The solid (dotted) shadings indicate clockwise (counter-clockwise) flow. The solid (dotted) contour lines are positive (negative) anomalies, and the zero lines are thickened. The dark spots indicate statistically significant anomalies at the 0.05 level based on the two-sided Student's *t* test. The global area is divided into three regions, including the Indo-Pacific Warm Pool (IPWP, 39° to 139°E), centraleastern Pacific (CEP, 139.5°– 270°E), and Atlantic (ATL, 90°W–39°E) regions.

energy dynamics, particularly the generation of *PPE*, are fundamentally influenced by the underlying spatial variations in SSTA.

The conversion of atmospheric PPE into kinetic energy is primarily mediated by the mid-term C_k^{45} (Atmospheric Perturbation Potential Energy, Methods). Under conditions where cold air ascends or warm air descends, C_k is positive, indicating a conversion from perturbation kinetic energy (PKE) to atmospheric PPE. In contrast, when warm air ascends or cold air descends, C_k becomes negative, denoting a transformation from atmospheric PPE to PKE⁴⁶. During RD events (Fig. 2c), regions exhibiting pronounced conversion from PPE to PKE are predominantly situated over the IO, WPWP region, southern of the CEP region. These areas align with the distribution of positive SSTA (spatial correlation coefficient of -0.56, p < 0.01) and are associated with enhanced diabatic heating. This signifies that more energy, generated as PPE from these heat sources, is readily available for conversion to PKE, fueling strong low-level convergence and upward airflows. Notable negative anomalies manifest in the NWP and along the western coast of the United States, indicative of significant upward movement of warm and moist air masses in these areas. In contrast, during the SD event, these regions predominantly demonstrate a conversion from PKE to PPE (Fig. 2d), with the focal point of upward movement of warm and moist air masses located in the CEP regions along the equator, exhibiting an approximately symmetrical configuration around the equator. And the spatial correlation coefficient between the C_k anomalies and SSTA reaches -0.63 (*p* < 0.01) during this event.

Furthermore, the zonal-mean C_k anomalies exhibit distinct vertical structures across different events. During RD events, the C_k anomalies display an equatorial asymmetric structure, with negative anomalies south of the equator and positive anomalies to the north (Fig. 2e), indicating a significant diabatic heating process⁴⁷ south of the equator. In contrast, during SD events, C_k anomalies show an equatorial quasi-symmetric structure with its maximum anomalies at the equator (Fig. 2f), suggesting that the center of latent heat release is situated at the equator ⁴⁵. Moreover, results from Japanese 55-year Reanalysis (JRA55) and the National Centers for Environmental Prediction/National Center for Atmospheric Research

Reanalysis 1 (NCEP1) (*Datasets, METHODS*) are consistent with the above findings (Supplementarys Figs. 4 and 5). These distinctive features imply that different tropical circulation responses may occur. Therefore, how do these changes in the conversion of atmospheric *PPE* to *PKE* affect tropical meridional circulation?

Impacts on the meridional circulation

We utilize the European Centre for Medium-Range Weather Forecasts Reanalysis v5 (ERA5, Datasets, METHODS) to calculate the mass stream function (MSF; Global HC, METHODS), allowing for spatial characterization of the HC. The climatological HC (Fig. 3a, shading) exhibits an equatorially quasi-symmetric structure, with one updraft branch at approximately 7°N and two downdraft branches near 30°N/S^{48,49}. A significant transition in their spatial distribution from RD to SD events is evident (Fig. 3a, b). During RD events, the MSF anomalies exhibit an equatorially asymmetric structure, negatively correlating with climatological MSF (R = -0.31, p < 0.05). Positive anomalous MSF is observed in the tropics, indicating an anomalous clockwise meridional circulation. In contrast, SD events display an equatorially quasi-symmetric anomalous pattern that resembles the climatological annual-mean pattern, showing a significant positive spatial correlation with climatological MSF within the range of 20°N to 20°S (R = 0.23, p < 0.05). Notably, the position of the zero contour shifts southward during SD events compared to climatology, indicating a southward displacement of the rising branch of the HC⁵⁰. The differences in HC between RD and SD events show a roughly symmetric pattern around the equator (Supplementary Fig. 6), with positive (negative) anomalies in the SH (NH). This indicates an intensification of the HC is expected in both the cells in the SH and NH during SD events.

Furthermore, the ascending branch of the anomalous HC is located near 10° S during RD events, whereas it shifts to the equator during SD events. The locations of the anomalous ascending branches align with the maximum of zonal-mean SSTA (Fig. 1c) and the minimum of zonal-mean C_k anomalies (Fig. 2e, f), respectively. This raises the question: why do global HC anomalies exhibit asymmetry in the upward branch between RD and

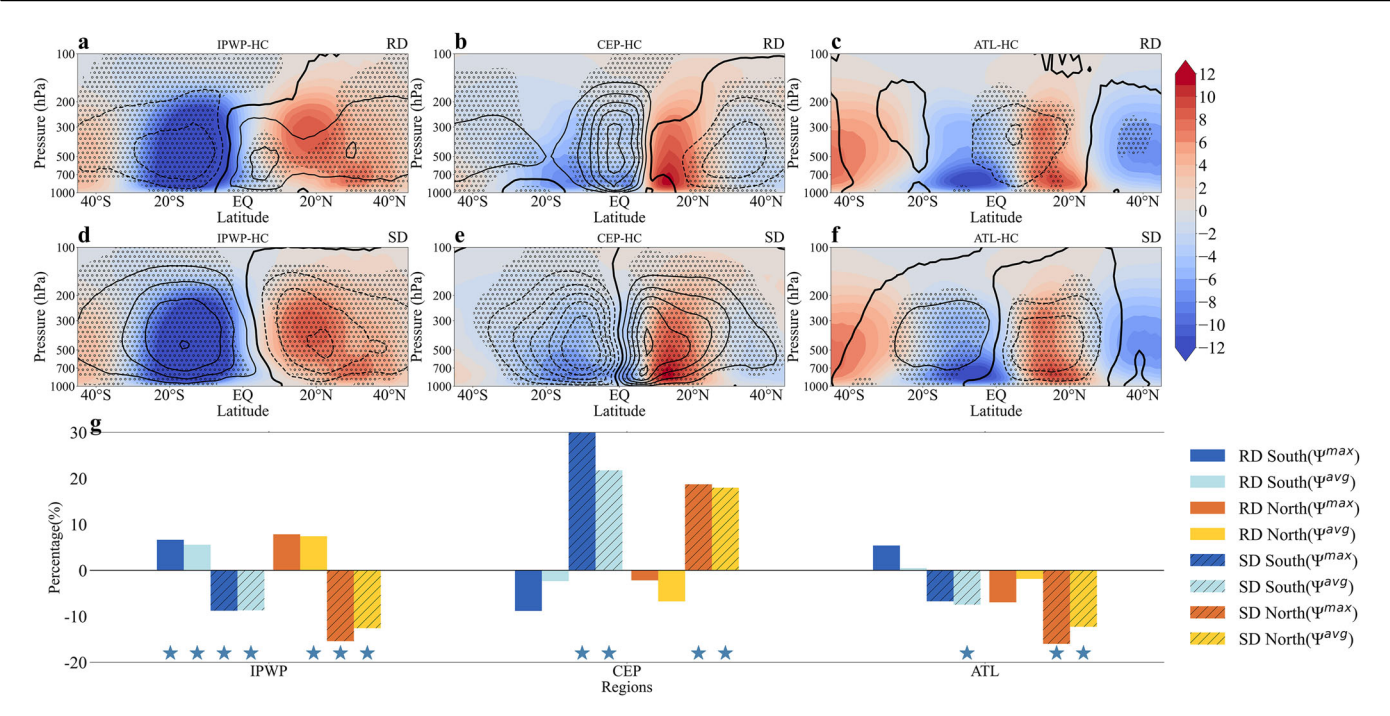


Fig. 4 | Spatial distribution of regional Hadley Circulation (HC) based on ERA5 dataset from 1950 to 2022 during RD and SD events. Composite differences of regional annual mean MSF anomalies averaged over IPWP (a), CEP (b), and ATL (c) regions during RD events (contour line, with an interval of $0.2 \times 10^{10} \, \text{kg·s}^{-1}$) and its climatological mean (shading, with an interval of $2 \times 10^{10} \, \text{kg·s}^{-1}$). The solid (dotted) contour line is positive (negative), and the zero line is thickened. d–f same as in (a–c), but during SD events. g The variations of annual mean HC intensity in the NH and SH cells of regional HC over IPWP, CEP, and ATL regions, respectively. Red and

yellow bars without slash indicates the anomalous HC intensity in the NH cell using two indices: Ψ^{max} defined as the maximum value at 500 hPa and Ψ^{avg} defined as the areal averaged value (HC intensity, METHODS) during RD events, respectively. Blue and cyan bars without slash, same as red and yellow bars, but for the results of the SH cell during RD events. The bar with slash indicates the results during SD events. The dark spots in a-f and blue stars in g indicate statistically significant anomalies at the 0.05 and 0.1 level using the two-sided Student's t test, respectively.

SD events? By simplifying the linearization formula relating underlying thermal conditions to low-level atmospheric circulation $(||v|| \propto \frac{\partial ||T_s||}{\partial \theta})^{27}$, we find a positive relationship between meridional wind and the zonal-mean SSTA gradient, implying that low-level convergence is subjected to the meridional SSTA gradients. Consequently, the position where the SSTA gradient varies from positive to negative coincides with the location of convergence. During RD events, the zero-crossing of the meridional gradient of zonal-mean SSTA occurs near 10°S (Fig. 1d), which coincides with the latitude of the meridional wind reversal (Supplementary Fig. 7a). Within the 10°S-10°N band, the anomalous meridional wind predominantly exhibits northerly anomalies, consistent with an anomalous southward flow in the low-level and forming a clockwise meridional circulation, thereby identifying the convergence zone associated with the HC's ascending branch at 10°S. Conversely, during SD events, these features appear near the equator, where the SSTA meridional gradient zero-crossing (Fig. 1d) and meridional wind sign reversal coincide (Supplementary Fig. 7b), explaining the anomalous ascending branch of the HC being situated near the equator. Furthermore, meridional wind anomalies exhibit southerlies south of the equator and northerlies north of it, corresponding to two distinct anomalous HC branches in the SH and NH (Fig. 3b).

Thus, El Niño RD and SD events result in significantly differences in the spatial distribution of global HC. This finding is strongly corroborated by results from NCEP1 and NOAA-20C datasets (Supplementary Figs. 8 and 9). Furthermore, the robustness of these anomalous HC spatial patterns is confirmed by two alternative RD and SD event definitions (Supplementary Figs. 10–14), indicating their insensitivity to the specific event classification (RD and SD events, Methods). These observed significant differences in SSTA and C_k across various ocean basins raise the question: What are the corresponding variations in the regional HC during RD and

SD events, and their irrespective role in contributing to the formation of global HC anomalies?

Which region dominates the global HC anomalies?

To understand the predominant regions influencing the global HC anomalies, we analyze the horizontal distribution of regional HC anomalies (*Regional HC, METHODS*) (Fig. 3c, d). Combining the distributions from both events, the regional HC can be partitioned into three cells.

The first localized HC is in the IPWP region (IPWP in Fig. 3c, d), exhibiting a clockwise (anticlockwise) circulation anomaly in the NH and an anticlockwise (clockwise) circulation anomaly in the SH during RD (SD) events. The corresponding vertical structures of the regional HC, derived from the divergent component of the meridional wind averaged over the IPWP, demonstrate an equatorially symmetric configuration through both events (Fig. 4a, d), albeit with opposite directions, indicating an enhancement (diminishment) of the regional HC during RD (SD) events. Spatial correlation analysis of the IPWP HC with SSTA reveals that anomalous SST variations in the WPWP region are the primary drivers of the observed contrasting HC spatial structures (Supplementary Fig. 15). During RD events, positive SSTA over the WPWP significantly enhances atmospheric diabatic heating, characterized by positive PPE anomalies (Fig. 2a). This vigorous heating triggers a Gill-type response^{51,52}, generating AAC in the upper troposphere over the IPWP and driving strong divergence. This circulation pattern, marked by low-level convergence (indicated by negative C_k anomalies in Fig. 2c) and extratropical subsidence, completes the meridional overturning cells, leading to a clockwise HC anomaly in the NH and an anticlockwise anomaly in the SH. Conversely, during SD events, persistent cold SSTA over the WPWP weakens diabatic heating, or even induces cooling, exhibiting negative PPE anomalies (Fig. 2b). This cooling drives anomalous high-level convergence and downwelling, with a

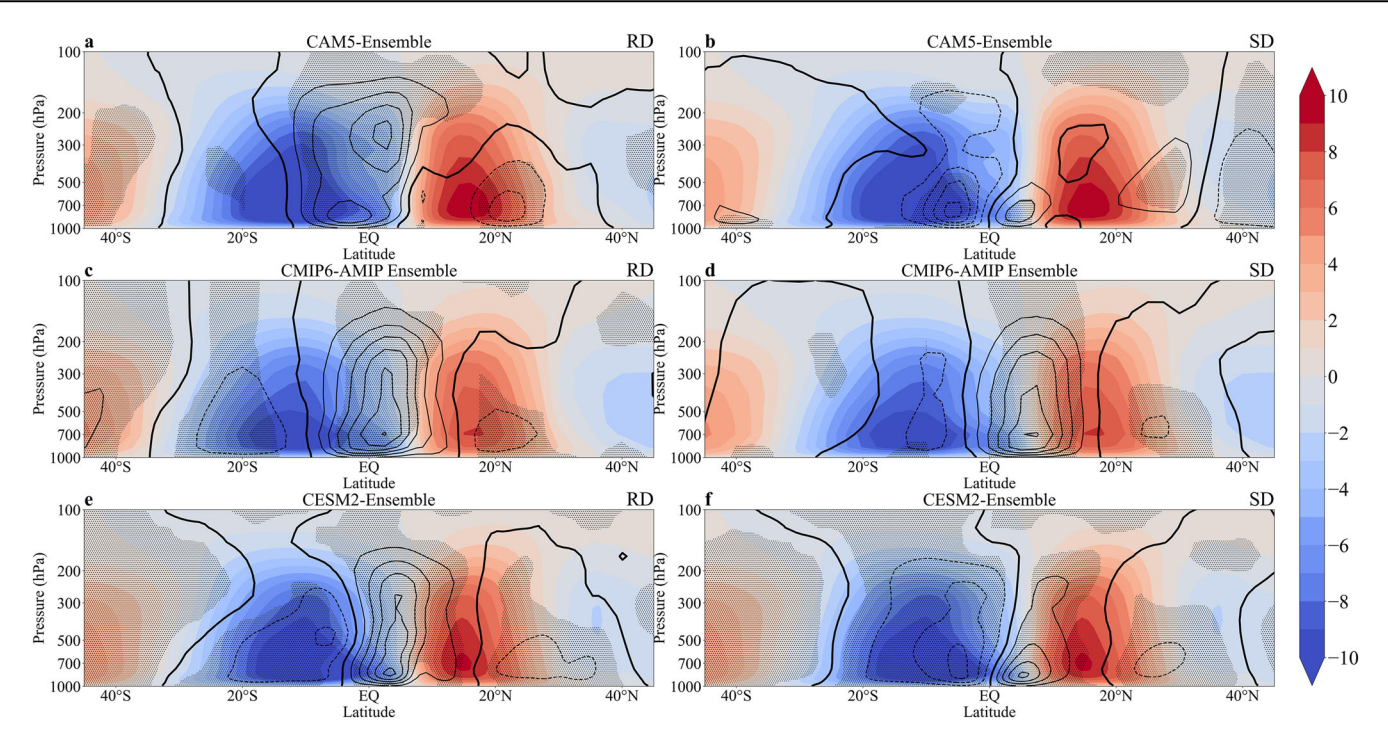


Fig. 5 | **Spatial distribution of the simulated HC. a**, **b** Composite differences of annual mean MSF anomalies (contour line, with an interval of $0.1 \times 10^{10} \, \text{kg·s}^{-1}$) and its climatological mean (shading, with an interval of $2 \times 10^{10} \, \text{kg·s}^{-1}$) based on CAM5 modeled results during the RD (**a**) and SD (**b**) events forced by SSTA over the CEP. **c**, **d** same as in (**a**, **b**), but for the results based on CMIP6-AMIP ensemble field from

1950 to 2013. **e**, **f** same as in (\mathbf{a}, \mathbf{b}) , but for the results based on CESM2 ensemble field from 1950 to 2019. The solid (dotted) contour line is positive (negative), and the zero line is thickened. The dark spots indicate statistically significant anomalies at the 0.05 level using two-sided Student's t test.

corresponding positive C_k anomaly (Fig. 2d) signifying an energy conversion from kinetic energy to diabatic heating. This process results in an anticlockwise HC anomaly in the NH and a clockwise anomaly in the SH, which weakens local upwelling and the regional HC strength. Previous studies suggest that El Niño decay events can weaken the HC over the IPWP⁵³. Our results diverge from this established pattern, highlighting the need for a nuanced examination of El Niño occurrences as distinct events characterized by varying rates of decay.

The second pair of cells is located in the CEP region (*CEP* in Fig. 3c, d), presenting different horizontal structures between the two events. Notably, positive MSF anomalies extend across the tropical region, suggesting a reduction in the intensity of regional HC in both hemispheres during El Niño RD events. The vertical structure of the regional HC shows an equatorially asymmetric feature (Fig. 4b). In contrast, during SD events, the regional HC exhibits an equatorially symmetric structure, with negative anomalies in the SH and positive anomalies in the NH (Fig. 4e). The anomalous regional HC over the CEP resembles the spatial patterns of global HC anomalies in both RD and SD events.

The third pair, positioned over the tropical Atlantic (*ATL* in Fig. 3c, d), signifies the distant impact of El Niño events, weakening the regional HC over the north Atlantic basin during both events (Fig. 4c, f). However, the HC anomalies in the southern Atlantic changes from negative to positive between RD and SD events.

Additionally, we analyze the maximum intensity variations in the SH and NH cells of the regional HC across three regions (*HC intensity, METHODS*). The two indices assessing HC intensity show coherence and consistency in their performance (Fig. 4g). Specifically, significant strengthening in the NH and SH cells over IPWP during RD events is detected. Conversely, during SD events, intensity anomalies exhibit contrasting behavior, showing weakening in both cells, with a greater amplitude than that during RD events. In the CEP, regional HC intensity in both the NH and SH cells decreases during RD events, while it amplifies during SD

events, particularly for the SH cell. In the ATL region, changes in regional HC intensity are negligible. During RD events, the NH cell weakens while the SH cell strengthens. However, both cells show weakening during SD events.

Thus, the presence of distinct decay events leads to diverse distribution features of regional HC. The spatial configuration of regional HC within the CEP region aligns closely with that of global HC. Therefore, from the perspective of spatial anomalies in HC across the three regions and globally, we hypothesize that the spatial anomalies of global HC during different El Niño decay events are primarily influenced by regional HC over the CEP.

We employ sensitivity experiment to validate the influence of SSTA over CEP region during RD and SD events on the global HC using the Community Atmospheric Model, version 5 (CAM5) (CAM5 model, METHODS). By incorporating monthly SSTA over tropical Pacific regions (Supplementary Figs. 16 and 17) into the corresponding month of the climatological SST field, we observe a similar equatorial asymmetric structure in the global HC during RD events (Fig. 5a) and a quasi-symmetric structure during SD events (Fig. 5b). This finding supports the conclusion that the CEP is the critical region influencing the HC during RD and SD events⁵⁴. It is noteworthy that disparities exist between the simulated HC anomalies and the observed HC anomalies (Fig. 3a,b), particularly for the extratropic. Discrepancies in the meridional circulation over the tropical NH compared to observations may be attributed to limited feedback mechanisms between the atmosphere and ocean⁵⁵, as well as the influence of NH landmasses on the air-sea interaction⁵⁶ using the CAM5 model. Further, the spatial correlation coefficients between simulated and observed patterns reach 0.71 (p < 0.05) for RD and 0.53 (p < 0.05) for SD events, both statistically significant. Additionally, it is evident that the horizontal distribution of regional HC anomalies (Supplementary Fig. 18) and their vertical anomalies (Supplementary Fig. 19) from the simulated results align closely with the observed results. To further corroborate these findings, we employ a 10-member ensemble of Community Earth System Model version 2

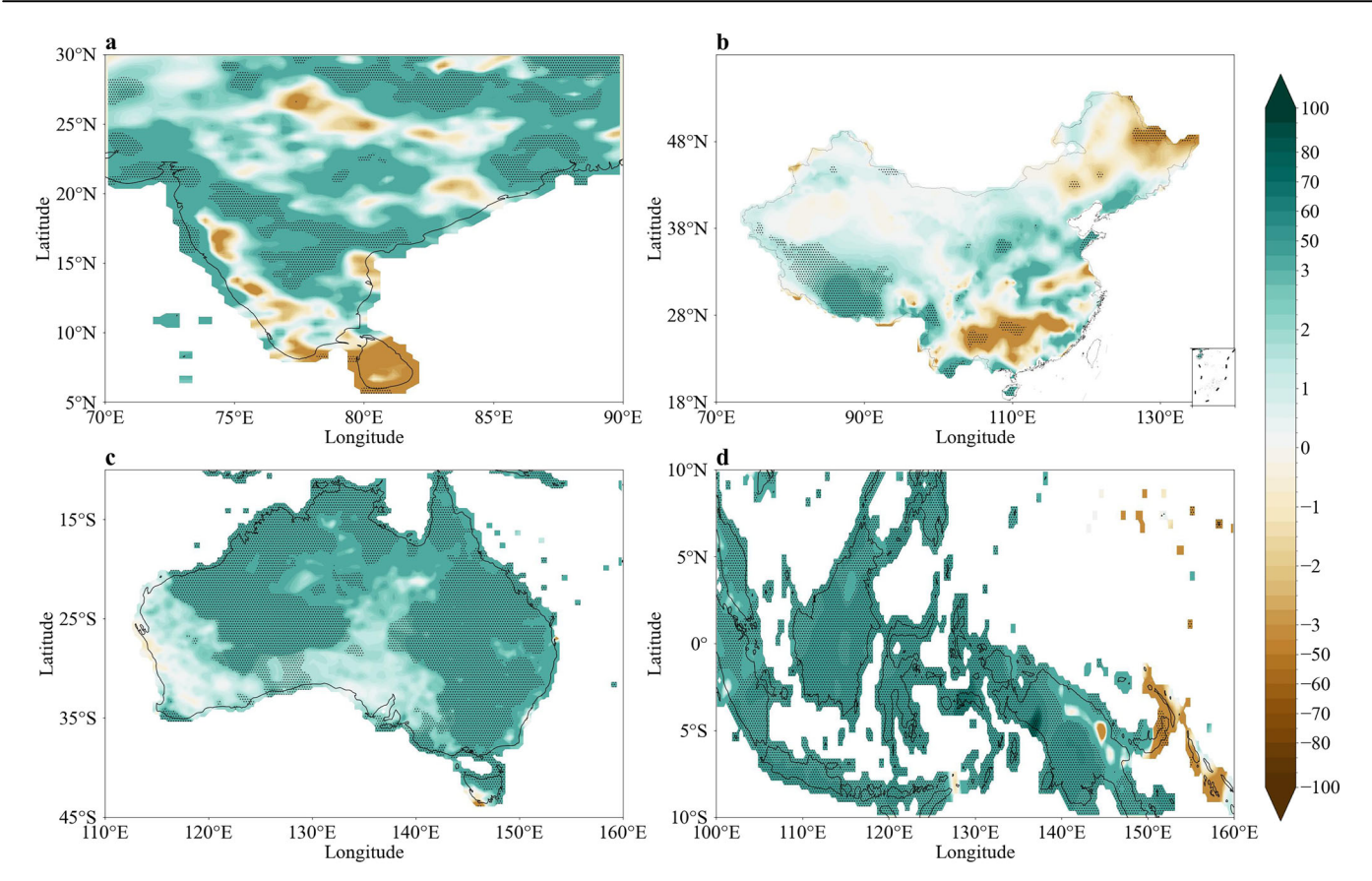


Fig. 6 | Impacts of IPWP HC on the South Asia-China-Australia-Maritime Continent land rainfall. Regression pattern of annual mean rainfall over South Asia (a), China (b), Australia (c), and Maritime Continent (d) against the annual mean IPWP HC intensity averaged over the NH cell and SH cell. As for South Asia, Australia, and Maritime Continent, the study period is the Global Precipitation

Climatology Centre (GPCC) dataset from 1950 to 2022, while for *China*, the study period is from 1961 to 2019 based on rainfall records from Chinese observation stations (units: mm·month⁻¹). The dark spots indicate statistically significant correlations at the 0.05 level using two-sided Student's *t* test.

(CESM2) simulations (*Datasets, METHOD*), which incorporate time-evolving SSTA in the eastern tropical Pacific⁵⁷ from 1950 to 2019. Additionally, we analyze output from 13 models participating in the Coupled Model Intercomparison Project Phase 6-Atmospheric Model Intercomparison Project (CMIP6-AMIP) from 1950 to 2013 (*Datasets, METHOD*). Consistent with the observations, the ensemble-averaged results exhibit analogous anomalous structures: an asymmetric structure during RD events (Fig. 5c, e) and a quasi-symmetric structure during SD events (Fig. 5d, f). Hence, the model results provide support that the variation of underlying SSTA over Pacific region exert significant influences on modulation the regional HC during both events.

To quantify this regional–global HC relationship, a further spatio-temporal correlation analysis between the global and regional HC anomalies was conducted (Supplementary Fig. 20). The correlation coefficient for RD events reaches 0.72 (p < 0.05), while for SD events it is 0.60 (p < 0.05), both indicating statistically significant coherence. This result confirms the significant contribution of CEP HC on the global circulation.

Impacts of regional HC on regional rainfall patterns?

The findings illustrate that the regional HC exhibits distinct spatial characteristics and varying intensities during RD and SD events. Given the HC's crucial role in influencing regional precipitation^{8,58,59}, it is important to assess the impacts of the opposing changes in the intensity of regional HC on the regional climate. Considering the similarities between regional anomalies over the CEP and global HC anomalies, it is plausible that the impacts may also be analogous. Additionally, the alterations in the regional HC intensity over ATL are not significant, whereas the regional HC over IPWP shows

divergences compared to global HC anomalies. Consequently, we focus on elucidating the implications of the shifts in the regional HC intensity within the IPWP on precipitation patterns in the South Asia-China-Australia-Maritime Continent region. To comprehensively capture the sustained modulation of the IPWP HC intensity on year-round climate responses, particularly cross-equatorial and interhemispheric teleconnections, this study was conducted. Monthly global precipitation data from the Global Precipitation Climatology Centre (GPCC⁶⁰) is utilized, combined with rainfall records from Chinese meteorological observation stations, to investigate its regional climatic impacts. Hence, the regression patterns of land rainfall anomalies in these regions relative to regional HC intensity over the IPWP are illustrated in Fig. 6.

Remote impacts—South Asia and China. During RD events, *South Asia* exhibits a pronounced anomalous increase in rainfall, notably concentrated over central India, Bangladesh, and the southern slopes of the central Himalayas (Supplementary Fig. 21a). Conversely, SD events are associated with widespread precipitation suppression across these regions, with only southern India and Sri Lanka showing localized, marginally positive rainfall anomalies (Supplementary Fig. 21e). These contrasting anomalous rainfall patterns over *South Asia* are generally overlapped with the IPWP HC intensity related rainfall areas (Fig. 6a). Specifically, regression analysis of *South Asian* rainfall anomalies against IPWP HC intensity shows statistically significant positive correlations. This correlation distribution shows a significant positive field correlation with the rainfall anomalous pattern during RD events (R = 0.65, p < 0.05), whereas it is negative (R = -0.45, p < 0.05) during SD events during SD

events. This relationship is consistent with the well-established influence of the cross-equatorial HC on the Asian monsoon system 61,62. Furthermore, the notably intensified *South Asian* summer monsoon response observed during RD events may significantly contribute to the occurrence of severe rainfall across the region 16,63,64. Mechanistically, an intensification of the IPWP HC strengthens the southeast trade winds in the southeastern IO. This, in turn, enhances the Mascarene High and modifies the water vapor transport flux, thereby influencing regional precipitation 8.

In addition, during RD events, widespread and significant heavy rainfall is observed across southwestern, central, eastern, and northern China (Supplementary Fig. 21b). Conversely, SD events are characterized by a distinct dipole rainfall distribution in eastern China, with abundant precipitation south of the Yangtze River basin and drought conditions north of the Yellow River basin (Supplementary Fig. 21f). This dipole pattern mirrors observations during boreal summer seasons of El Niño decay years^{65,66}. Regression analysis of rainfall anomalies against the IPWP HC intensity reveals a positive correlation with rainfall in southwestern and northeastern China, and negative correlations in southeastern China and Tibet (Fig. 6b). Consequently, this rainfall pattern demonstrates a statistically significant negative correlation with the spatial distribution of rainfall anomalies during SD events (R = -0.44, p < 0.05), and a significant positive correlation during RD events (R = 0.36, p < 0.05). While previous studies have emphasized the role of AAC variability on East Asia during different El Niño decay phases13 -15, the robust correlation in the *China* rainfall anomalies between those during the RD/SD events and associated with IPWP HC intensity underscores a direct influence of regional HC intensity on precipitation patterns over China.

Remote impacts—Australia and Maritime Continent. Precipitation patterns in Australia and the Maritime Continent exhibit a direct correlation with anomalous tropical SST⁶⁷. Various El Niño occurrences result in distinct degrees and spans of precipitation irregularities^{3,20}. Consequently, these regions display distinct spatial distribution characteristics of rainfall anomalies under varying decay rates, demonstrating significantly strengthened precipitation during RD events and weakened precipitation during SD events (Supplementary Fig. 21). Moreover, regression analysis of rainfall against IPWP HC intensity reveals significant rainfall increases, particularly in inland and eastern Australia (Fig. 6c), and across much of the Maritime Continent (Fig. 6d). This regressed pattern closely resembles the observed rainfall anomalies during SD events, evidenced by strong negative spatial correlation coefficients of -0.72 (p < 0.05) for Australia and -0.73 (p < 0.05) for the Maritime Continent. Conversely, a robust positive spatial correlation is observed with rainfall anomalies during RD events, with coefficients of 0.76 (p < 0.05) for *Australia* and 0.53 (p < 0.05) for the *Maritime Continent*. Therefore, an intensification of regional HC activity is consistently associated with positive anomalous rainfall in these regions, while its weakening leads to negative anomalies. These findings align with earlier research findings, which suggest heightened precipitation in northern Australia when the regional HC over the western Pacific is more robust³⁵, and further underscore the crucial role of regional HC on the rainfall during both RD and SD events.

Thus, distinct differences in regional rainfall anomalies are observed between El Niño decay types. RD events are associated with enhanced precipitation, while SD events exhibit suppressed rainfall, and in some regions (*Australia and the Maritime Continent*), severe drought. Additionally, we conducted the correlation between the IPWP HC intensity and precipitation but during the boreal summer (June–July–August, JJA). The result is similar to that as observed based on the annual mean (Supplementary Fig. 22-23). This result suggests that the variation of IPWP HC intensity may be an important driver of these contrasting rainfall anomalous patterns during RD and SD events.

Discussion

This study evaluates the impact of different decay rates of El Niño events on the tropical meridional circulation. We find the anomalous spatial structure of global HC performs an equatorial asymmetric (quasi-symmetric) feature during El Niño RD (SD) events (Fig. 3). From a global perspective, this is mainly driven by the meridional gradient of global zonal-mean SSTA⁶⁸. During RD events, energy conversion involves a significant transformation from PPE to PKE, primarily driven by diabatic heating processes⁴⁶ occurring in the southern part of the IPWP and the equatorial Pacific region. This results in an equatorially asymmetrical structure characterized by ascending of warm and moist air around 10°S (Fig. 2), leading to enhanced atmospheric meridional circulation⁴⁵. Conversely, during SD events, the conversion process shifts, with a notable transition from kinetic energy to atmospheric potential energy over the IPWP, alongside a significant conversion from potential energy to kinetic energy over the CEP. This scenario exhibits an equatorially quasi-symmetrical structure marked by upward of warm and moist air masses at the equator. These differences in energy conversion processes underscore the varying impacts of different decay rate of El Niño on the spatial structures of global HC anomalies by altering atmospheric stability⁶⁹ and circulation characteristics⁴⁵.

We find that the variation of the global HC is dominated by the regional HC over the CEP. During RD events, anomalous westerlies dominate the south of CEP, leading to positive SSTA (Fig. 7). Accordingly, this results in a diabatic heating process via latent heat release⁷⁰, driven by the enhanced SSTA. Consequently, the conversion of PPE to PKE generates anomalous upward airflow, determining the location of the anomalous ascending branch of the HC over the south of CEP (Fig. 7). In contrast, during SD events, positive SSTA persist within the CEP, but their maximum amplitude shifts towards the equator, resulting in anomalous ascending in the equator region. This finding is further validated based on the CAM5, CMIP6-AMIP, and CESM2 ensemble simulations, supporting that the variation of SSTA in the CEP is a decisive factor contributing to the global HC anomalies. Additionally, the spatial structure of IPWP HC exhibits contrasting structures during RD and SD events, primarily due to differing atmospheric diabatic heating anomalies over the WPWP and their associated Gill-type responses⁵².

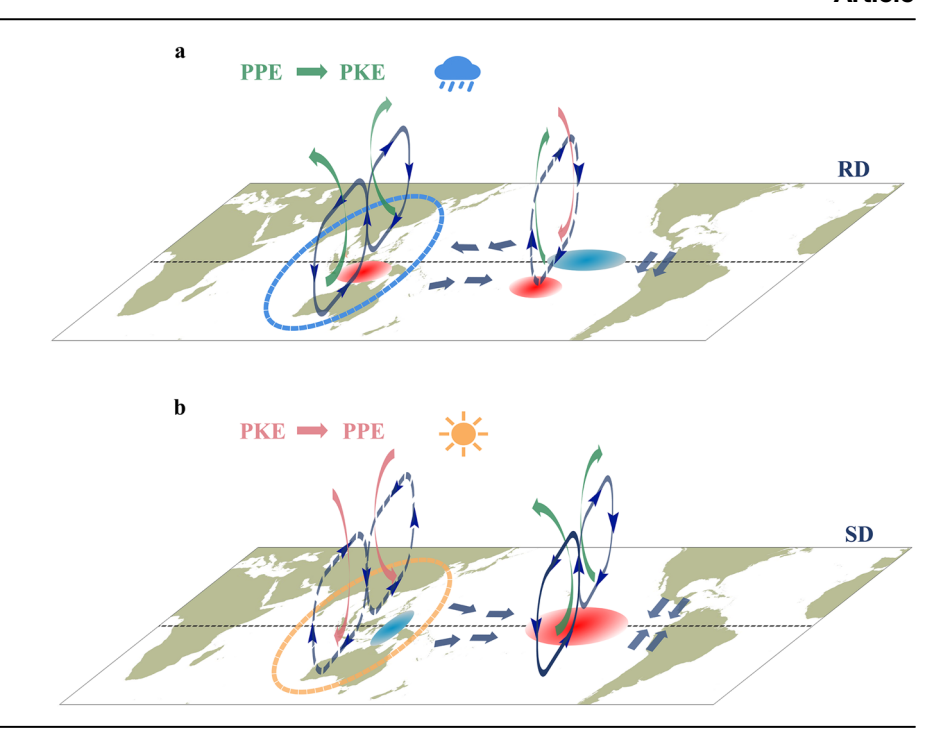
Moreover, the IPWP HC intensity are intensified during RD events, and suppressed during SD events (Fig. 4g). Our findings reveal an increase in IPWP HC intensity are accompanied with enhanced rainfall in the *South Asia-China-Australia-Maritime Continent* regions, while a decreased intensity is connected with reduced precipitation in these areas (Fig. 6). This robust connection highlights the crucial role of regional HC, particularly over the IPWP, in shaping regional rainfall anomalies during different El Niño decay events (Fig. 7). This offers a novel perspective for comprehending precipitation anomalies linked to varying El Niño decay rates in the IPWP vicinity. Crucially, given that climate models generally simulate large-scale circulation more reliably than local precipitation^{71–74}, the linkage between regional HC and rainfall presents a robust and interpretable candidate predictor for seasonal precipitation, thus holding significant potential for future practical prediction applications.

It is indicated that El Niño events are projected to persist for longer durations in the eastern and far eastern Pacific in the future²⁰. Additionally, it is noted that intense El Niño events often transition into RD events, and the frequency of these strong El Niño occurrences is anticipated to increase with global warming⁷⁵. Analysis of this study suggests that the IPWP vicinity regions may see elevated precipitation in the future under high-emission scenarios. Consequently, these results provide a novel perspective on understanding shifts in regional HC, its association with SSTA, and its impact on regional climate during different El Niño decay rates and their future projections.

Methods RD and SD events

During an El Niño event, the Niño 3.4 index, which represents the areal-averaged SSTA in the region of 170°–120°W and 5°S–5°N, exceeds 0.5 °C for

Fig. 7 | Schematic diagram depicting the influence of different El Niño decaying rates on the regional HC. (a) Schematic diagram for the RD event, and (b) schematic diagram for the SD event. Red shading indicates positive SSTA, while dark blue shading indicates negative SSTA. Enhanced regional HC is depicted by a solid blue circle with vectors, whereas weakened regional HC is represented by a dashed blue circle. Blue arrows represent zonal and meridional wind anomalies. Green arrows indicate negative C_k anomalies, signifying energy conversion from PPE to PKE. This pattern is associated with warm, moist air upwelling and suggests positive precipitation anomalies over the regions highlighted by the blue ellipse. Conversely, magenta arrows indicate positive C_k anomalies, signifying energy conversion from PKE to PPE. This pattern is associated with negative precipitation anomalies over the regions as shown within the orange ellipse.



a continuous period of 5 months or longer, indicating the occurrence of an El Niño episode. In total, 25 El Niño events were identified. To classify into the RD and SD events, two criteria^{12,19} are employed (Criterion-1). First is that the discrepancy between the most intense SSTA observed during the El Niño event and that in the subsequent June-August (JJA) period of the decay year surpasses 1 °C. Second is that the SSTA recorded during the decay year's JJA period is either less than or equal to 0.2 °C. Therefore, events meeting both criteria are categorized as RD El Niño events, while those that fall short are labeled as SD events. Notably, the El Niño event of 1982/ 83 satisfies the first criterion but not the second. However, considering that by 1983, the SST in the tropical Pacific region had reverted to mean conditions, it is considered as an RD event in this study. Consequently, 14 RD events (1951/52, 1953/54, 1963/64, 1969/70, 1972/73, 1977/78, 1982/83, 1987/88, 1994/95, 1997/98, 2002/03, 2006/07, 2009/10, 2015/16) and 11 SD events (1957/58, 1958/59, 1965/66, 1968/69, 1976/77, 1979/80, 1986/87, 1991/92, 2004/05, 2014/15, 2018/19) are identified. In this paper, a composite method is used to extract features common to RD and SD events. The statistical significance of the findings was assessed using two-sided Student's t test. Notably, the period from 1950 to 2022 included several sequences of consecutive El Niño events (1957/59, 1968/70, 1976/78, 1986/88, and 2014/ 16). To address potential uncertainties arising from these events, we performed a supplementary analysis excluding these periods (Supplementary Figs. 10 and 11). Additionally, a sensitivity analysis is also performed to categorize El Niño events as fast-decaying or slow-decaying. Additionally, we use the criterion that an El Niño event is considered fast-decaying if the Niño-3.4 index in the subsequent June-July-August (JJA) period is less than 0 (Criterion-2). This definition identifies (1951/52, 1953/54, 1958/59, 1963/ 64, 1969/70, 1972/73, 1977/78, 1982/83, 1987/88, 1994/95, 1997/98, 2004/ 05, 2006/07, 2009/10, 2015/16) as RD events and (1957/58, 1965/66, 1968/ 69, 1976/77, 1979/80, 1986/87, 1991/92, 2002/03, 2014/15, 2018/19) as SD events. However, years where the two methods disagreed (1958/59, 2002/03, and 2004/05) are excluded to maintain classification consistency. Therefore, the events identified using the two methods align. Moreover, to address potential uncertainties arising from different classification methods, we further perform a supplementary analysis under Criterion-2 method and excluding these disagreed events (Supplementary Figs. 12 and 13). Moreover, we further calculated the Niño 3.4 index decay rate for each event defined as Criterion-3 method. The specific method is as follows: 1) determine the month when the event reaches its maximum intensity. 2) select the Niño 3.4 index until the summer (JJA) of the decay year. Finally, apply linear fitting to the SSTA changes during this period, with the fitted slope defined as the decay rate of the event (Supplementary Fig. 24). Using the median decay rate of the 25 events, we classified them into 14 RD (1951/52, 1953/54, 1957/58, 1963/64, 1965/66, 1969/70, 1972/73, 1982/83, 1987/88, 1997/98, 2002/03, 2006/07, 2009/10, 2015/16) and 11 SD events (1958/59, 1968/69, 1976/77, 1977/78, 1979/80, 1986/87, 1991/92, 1994/95, 2004/05, 2014/15, 2018/19). Under this classification, 12 RD events overlap with those identified by the 1.0 °C and 0.2 °C threshold criteria, and 9 SD events overlap, yielding an overlap rate exceeding 75%. A similar spatial structure of the global and regional HC can be captured using Criterion-3 method (Supplementary Fig. 14). Therefore, these evidences strengthen our confidence in our conclusions.

Datasets

The spatial variability of the HC under various El Niño decay events is examined by analyzing monthly-mean meridional wind from three atmospheric reanalysis datasets: the National Centers for Environmental Prediction/National Center for Atmospheric Research Reanalysis 1 (NCEP1⁷⁶), European Centre for Medium-Range Weather Forecasts (ECMWF) Reanalysis v5 (ERA5⁷⁷) covering the period 1950-2022, Japanese 55 year Reanalysis (JRA55⁷⁸) from 1958 to 2022, and the National Oceanic and Atmospheric Administration (NOAA-20C⁷⁹) dataset spanning from 1950 to 2015. Additionally, the monthly-mean air temperature, relative humidity, vertical velocity, and sea level pressure from NCEP1 are employed to compute atmospheric perturbation energy, enabling an assessment of the physical mechanisms driving the variations in tropical meridional circulation and energy conversion processes. Monthly-mean global precipitation data from the Global Precipitation Climatology Centre (GPCC⁶⁰) over the period 1950-2022, along with rainfall records from Chinese observation stations over the period 1961-2019, are utilized to examine regional climatic effects. Moreover, we also use the gridded daily rainfall data provided by the Global Precipitation Climatology Project (GPCP) with a horizontal resolution of 2.5° from 1979 to 202280. Additionally, the NOAA Extended Reconstructed Sea Surface Temperature v5 (ERSST5⁸¹) oceanic dataset is utilized to capture sea surface temperature variations. To validate the observed results, we utilized the Community Earth System Model version 2 (CESM2) Pacific Pacemaker Ensemble datasets. This ensemble comprises 10 simulations, in which time-evolving SSTA in the eastern tropical Pacific

(10°S–10°N, 160–90°W) are nudged to ERSSTv3b datasets during 1920–2019. A linearly tapering buffer zone extends the nudging region to 20°S and 20°N from 180°W to the American coast 57 . Additionally, we analyze output from 13 models participating in the Coupled Model Intercomparison Project Phase 6-Atmospheric Model Intercomparison Project (CMIP6-AMIP) during 1950–2013 (Supplementary Table 1). The ensemble average over 13 models is derived by interpolating them into the same horizontal resolution of 2.5° × 2.5°. Given the time range of the CMIP6-AMIP ensemble, RD events do not include 2015, and SD events exclude 2014 and 2018.

Global zonal-mean HC

The mass stream function (MSF, ψ) to quantify the mean meridional circulation, which is mainly obtained by integrating the meridional wind in the vertical direction as follows:

$$\Psi(\phi, p) = \frac{2\pi R \cos \phi}{g} \int_{p_0}^{p} [\bar{\nu}(\phi, p)] dp \tag{1}$$

where ψ is the MSF, ϕ is the latitude, p is the pressure, g (9.80665 m s⁻²) is gravitational acceleration, v stands for the zonal-mean meridional wind, R is the Earth's radius, and overbar and square brackets represent temporal and zonal averaging, respectively. A positive meridional overturning circulation signal (typically occurring over the Northern Hemisphere, NH) is characterized by a clockwise pattern with rising at the equator and sinking in the subtropical regions of the NH. Conversely, a negative signal in meridional overturning circulation represents an anticlockwise pattern of circulation s².

Regional HC

According to the Helmholtz theorem, the horizontal wind field can be decomposed into two parts: the non-divergent part $V_{_{Y}}$ and the non-rotating part $V_{_{Y}}$,

$$V = V_{yy} + V_{y} \tag{2}$$

Therefore, to assess the role of regional HC on the global meridional circulation, the regional HC calculation method⁸³ is obtained by integrating the divergent component of the meridional wind as follows:

$$\Psi_R(x, y, p) = \frac{2\pi R \cos \phi}{g} \int_{p_0}^{p} [\bar{\nu_\chi}(x, y, p)] dp$$
 (3)

where Ψ_R is the regional MSF. According to this approach, we initially break down the horizontal velocity at every pressure level to determine the non-divergent part and non-rotational velocity. Subsequently, we integrate the divergent component from the upper atmosphere to the surface at each point of longitude to derive the three-dimensional HC. To characterize the regional HC, the meridional MSF is derived by averaging the divergent component of the meridional wind in a regional domain. In this paper, the regional HC can be partitioned into three cells, including IPWP region (39°–139°E), CEP (139.5°–270°E), and tropical Atlantic region (90°W–39°E).

HC intensity

To assess the influence of different decay rates of El Niño event on the HC intensity, two distinct definitions of HC strength are utilized within this research. The initial definition characterizes HC strength as the highest absolute value of Ψ at 500 hPa in each hemisphere (Ψ^{max})⁸⁴. The second interpretation involves computing the spatially averaged HC strength by averaging the stream function field across the latitude-pressure plane⁸⁵. In defining the HC intensity in the NH, the following criteria are employed:

$$\Psi_{NH}^{avg} = \left[\Psi(\phi, p)\right] \begin{cases} \Psi(\phi, p) > 0 \\ \left(\phi, p\right) \in \left[-15^{\circ}, 45^{\circ}\right] \times [100, 1000] hPa \end{cases}$$
(4)

For the HC intensity in the Southern Hemisphere, it is defined as follows:

$$\Psi_{SH}^{avg} = \left[\Psi(\phi, p)\right] \begin{cases} \Psi(\phi, p) < 0 \\ \left(\phi, p\right) \in \left[-45^{\circ}, 20^{\circ}\right] \times [100, 1000] hPa \end{cases}$$
 (5)

where Ψ is sampled uniformly across latitude and at vertical intervals of 50hPa.

Walker circulation

Following previous work⁵⁰, the WC is defined as follows:

$$\Psi_{WC}(\lambda, p) = \frac{2\pi R}{g} \int_{p_0}^{p} u_D dp \tag{6}$$

where Ψ_{WC} is the zonal circulation, λ is the longitude, u_D stands for divergent component of zonal wind averaged over the tropics (5°S–5°N).

Atmospheric perturbation potential energy

Regarding the issue of energy conversion in local circulation, we employ atmospheric PPE and conversion terms (C_k) to analyze the spatial distribution characteristics of energy. The PPE provides a localized perspective on the conversion dynamics between diabatic heating and kinetic energy. The mathematical expression for $PPE^{45,46}$ is as follows:

$$PPE = \sum_{i=1}^{\infty} PPE_i = \sum_{i=1}^{\infty} \frac{p_{00}^{(i-1)\kappa} \prod_{j=01}^{i=1} (1+\kappa-j)}{i! \gamma_d (1+\kappa)} \int_0^{p_s} \frac{T'^{i}}{p^{(i-1)(1+\kappa)}} (-\frac{\partial \bar{\theta}}{\partial p})^{-i+1} dp$$
(7)

where i is the order terms of PPE. p, p_{00} , and p_s are the pressure, reference pressure (generally 1000hPa), and surface pressure, respectively. $\kappa = R/C_p$, where R (287 J kg⁻¹ K⁻¹) and C_p (1004 J kg⁻¹ K⁻¹) are the gas constant of dry air and the specific heat at a constant pressure, respectively. $y_d = g/C_p$ indicates the dry adiabatic lapse rate. $\bar{\theta}(K)$ is the potential temperature at reference state, and T'(K) denotes the departure of air temperature after removing the area-weighted seasonal cycle. Thus, the mathematical expressions of the first and second moment terms of PPE can be written as:

$$PPE_1 = \frac{1}{\gamma_d} \int_0^{\rho_s} T' dp \tag{8}$$

$$PPE_2 = \frac{\kappa p_{00}^{\kappa}}{2\gamma_d} \int_0^{p_s} \frac{T^{\prime 2}}{p^{(1+\kappa)}} \left(-\frac{\partial \bar{\theta}}{\partial p}\right)^{-1} dp \tag{9}$$

where PPE_1 and PPE_2 denote the first and second order terms of PPE, respectively. In contrast to PPE_1 and PPE_2 , the higher-moment terms of PPE are much smaller and can be omitted at the local scale (Supplementary Table 2). Thus, atmospheric PPE is calculated as the sum of PPE_1 and PPE_2^{-46} .

The energetic conversion between the atmospheric *PPE* and perturbation kinetic energy (*PKE*) is mainly controlled by the following equations:

$$\frac{1}{g} \int_{0}^{p_{s}} \frac{\partial PPE}{\partial t} dp = C_{\kappa} + G + HBF_{PPE}$$
 (10)

$$\frac{1}{g} \int_{0}^{p_s} \frac{\partial PKE}{\partial t} dp = -C_{\kappa} + D + HBF_{PKE}$$
 (11)

Where *G*, *D*, and *HBF* denote the diabatic heating, viscous dissipation, and horizontal boundary fluxes, respectively. A detailed derivation of the local thermodynamic equation and the local kinetic energy equation is shown in Supplementary Text 1. *G* is the source term of *PPE*, representing diabatic

heating. When there is a positive anomalous heating locally, it increases PPE, whereas a negative anomalous heating results in a depletion of PPE. Therefore, the atmospheric diabatic heating G term in Eq. 10 does not directly alter PKE; instead, it first modifies PPE according to the governing equations. Consequently, PPE serves as a crucial intermediary that links diabatic heating to changes in atmospheric circulation. Previous studies have shown that the energy exchange between PPE and PKE is mainly achieved through the conversion term $C_k^{45,46}$, as detailed in the following formula:

$$C_k = \frac{1}{g} \int_0^{P_s} \omega a dp \tag{12}$$

where ω is the pressure velocity, and a is air specific volume. When cold air ascends or warm air descends, C_k is positive and energy is converted from *PKE* to *PPE*. Conversely, when warm air ascends or cold air descends, C_k is negative, and *PPE* is converted to *PKE*.

CAM5 model

To further corroborate the proposed mechanism concerning the impact of SST on the HC during the two events of El Niño, we utilized the Community Atmospheric Model, version 5 (CAM5), developed by the National Center for Atmospheric Research (NCAR). The CAM5 serves as a comprehensive global climate model and constitutes the atmospheric component within the NCAR Community Earth System Model (CESM). With a horizontal resolution measuring $1.9^{\circ} \times 2.5^{\circ}$ and consisting of 30 vertical layers, CAM5 possesses the capacity to accurately replicate various climatic characteristics. A full description of CAM5 is available online at https://ncar.github.io/CAM/doc/build/html/cam5 scientific guide/.

Here, three experiments are carried out, with the first being a free-run experiment driven by the climatological SST field as the model's baseline. The second set entails incorporating monthly SSTA during the RD events (Supplementary Fig. 16) into the respective month of the climatological SST field, while the third set involves incorporating monthly SSTA during the SD events (Supplementary Fig. 17) into the corresponding month of the climatological SST field. To address potential issues of model instability or "spillover" caused by abrupt SSTA boundaries, we applied a non-orthogonal spatial filtering procedure to the added SSTA. This filtering employed a decay rate of one-fifth within 5° latitude of the boundary edges to ensure smooth transitions and maintain numerical stability in the simulations. Each experimental group comprises 22 years of numerical simulations. Then, we perform ensemble averaging on the results from the 3rd year to the 22nd year for each set of experiments, thus obtaining the corresponding climatological distribution of the HC.

Data availability

The data for atmosphere used in the manuscript are publicly available for NCEP1 (https://psl.noaa.gov/data/gridded/), JRA55 (https://rda.ucar.edu/ data-sets/ds628.1/dataaccess/), NOAA-20C (https://climatedataguide.ucar. edu/climate-data/noaa-20th-century-reanalysis-version-2-and-2c), ERA5 (https://www.ecmwf.int/en/forecasts/dataset/ecmwf-reanalysis-v5). the SST data is publicly available for ERSST5 (http://www.esrl.noaa.gov/ psd/data/gridded/). The index for the El Niño events definition is publicly available https://origin.cpc.ncep.noaa.gov/products/analysis_ monitoring/ensostuff/ONI_v5.php. The model data for CESM2 Pacific Pacemaker experiment is publicly available at https://rda.ucar.edu/datasets/ d651068/dataaccess/# and for the CMIP6-AMIP models is publicly available at https://esgf-node.llnl.gov/search/cmip6/. The data for precipitation are publicly available for GPCP (https://psl.noaa.gov/data/gridded/data. gpcp.html), GPCC (https://climatedataguide.ucar.edu/climate-data/gpccglobal-precipitation-climatology-centre), and for Chinese observation stations (https://data.cma.cn/data/detail/dataCode/A.0019.0001.S001.html).

Code availability

Any codes used in the manuscript are available upon request from iixl@nmefc.cn.

Received: 16 May 2025; Accepted: 28 August 2025; Published online: 13 October 2025

References

- Bjerknes, J. Atmospheric teleconnections from the equatorial Pacific. *Monthly Weather Rev.* 97, 163–172 (1969).
- Neelin, J. D. et al. ENSO theory. J. Geophys. Res. Oceans 103, 14261–14290 (1998).
- Capotondi, A. et al. Understanding ENSO diversity. Bull. Am. Meteorol. Soc. 96, 921–938 (2015).
- Timmermann, A. et al. El Niño-Southern oscillation complexity. *Nature* 559, 535–545 (2018).
- Chen, N., Fang, X. & Yu, J.-Y. A multiscale model for El Niño complexity. npj Clim. Atmos. Sci. 5, https://doi.org/10.1038/s41612-022-00241-x (2022).
- Chen, N. & Fang, X. A simple multiscale intermediate coupled stochastic model for El Niño diversity and complexity. J. Adv. Model. Earth Syst. 15, https://doi.org/10.1029/2022ms003469 (2023).
- Fang, X., Dijkstra, H., Wieners, C. & Guardamagna, F. A nonlinear full-field conceptual model for ENSO diversity. *J. Clim.* https://doi.org/10.1175/jcli-d-23-0382.1 (2024).
- Freitas, A. C. V., Aímola, L., Ambrizzi, T. & de Oliveira, C. P. Changes in intensity of the regional Hadley cell in Indian Ocean and its impacts on surrounding regions. *Meteorol. Atmos. Phys.* 129, 229–246 (2016).
- Guo, Y. P., Feng, X. B., Klingaman, N. P. & Tan, Z. M. Impact of Indo-Pacific warm pool Hadley circulation on the seasonal forecast performance for summer precipitation over the western North Pacific. *Environ. Res. Lett.* 15, https://doi.org/10.1088/1748-9326/aba97c (2020).
- Yang, X. K. & Huang, P. Restored relationship between ENSO and Indian summer monsoon rainfall around 1999/2000. *The Innovation* 2, https://doi.org/10.1016/j.xinn.2021.100102 (2021).
- Wu, R. G. & He, Z. Q. Northern Tropical Atlantic warming in El Niño decaying spring: impacts of El Niño amplitude. *Geophys. Res. Lett.* 46, 14072–14081 (2019).
- Chen, J. et al. Tropical and subtropical pacific sources of the asymmetric El Niño-La Niña decay and their future changes. *Geophys. Res. Lett.* 49, https://doi.org/10.1029/2022gl097751 (2022).
- Zhou, Q. & Wei, L. Influence of the pace of El Niño decay on tropical cyclone frequency over the western north Pacific during decaying El Niño summers. Atmos. Ocean. Sci. Lett. 16, https://doi.org/10.1016/j. aosl.2023.100328 (2023).
- Wu, M., Zhou, T. & Chen, X. The source of uncertainty in projecting the anomalous western North Pacific anticyclone during El Niño-decaying summers. J. Clim. 34, 1–49 (2021).
- Chen, W., Park, J. K., Dong, B., Lu, R. & Jung, W. S. The relationship between El Niño and the western North Pacific summer climate in a coupled GCM: Role of the transition of El Niño decaying phases. *J. Geophys. Res. Atmos.* 117, https://doi.org/10.1029/2011jd017385 (2012).
- Zhou, X. et al. Different responses of East Asian summer rainfall to El Niño decays. Clim. Dyn. 53, 1497–1515 (2019).
- Chowdary, J. S. et al. Tropical Indian Ocean response to the decay phase of El Niño in a coupled model and associated changes in south and east-Asian summer monsoon circulation and rainfall. *Clim. Dyn.* 47, 831–844 (2015).
- Kug, J.-S. et al. Role of the ENSO-Indian Ocean coupling on ENSO variability in a coupled GCM. Geophys. Res. Lett. 33, https://doi.org/10.1029/2005gl024916 (2006).
- Wu, J. et al. Boosting effect of strong western pole of the Indian Ocean Dipole on the decay of El Niño events. npj Clim. Atmos. Sci. 7, https://doi.org/10.1038/s41612-023-00554-5 (2024).

- Lopez, H., Lee, S.-K., Kim, D., Wittenberg, A. T. & Yeh, S.-W. Projections of faster onset and slower decay of El Niño in the 21st century. *Nat. Commun.* 13, https://doi.org/10.1038/s41467-022-29519-7 (2022).
- Lindzen, R. S. Climate dynamics and global change. Annu. Rev. Fluid Mech. 26, 353–378 (1994).
- 22. Hou, A. Y. Hadley circulation as a modulator of the extratropical climate. *J. Atmos. Sci.* **55**, 2437–2457 (1998).
- Trenberth, K. E. & Stepaniak, D. P. Seamless Poleward atmospheric energy transports and implications for the Hadley circulation. *J. Clim.* 16, 3706–3722 (2003).
- Zhang, G. & Wang, Z. Interannual variability of the Atlantic Hadley circulation in boreal summer and its impacts on tropical cyclone activity. J. Clim. 26, 8529–8544 (2013).
- Nguyen, H., Evans, A., Lucas, C., Smith, I. & Timbal, B. The Hadley circulation in reanalyses: climatology, variability, and change. *J. Clim.* 26, 3357–3376 (2013).
- Seager, R., Harnik, N., Kushnir, Y., Robinson, W. & Miller, J. Mechanisms of hemispherically symmetric climate variability*. *J. Clim.* 16, 2960–2978 (2003).
- Feng, J., Ji, X. L., Li, J. P. & He, E. Y. Asymmetric impacts of El Niño development and decay stages on the Hadley circulation. *Geophys. Res. Lett.* 50, https://doi.org/10.1029/2023GL103861 (2023).
- Oort, A. H. & Yienger, J. J. Observed interannual variability in the Hadley circulation and its connection to ENSO. *J. Clim.* 9, 2751–2767 (1996).
- Guo, Y. P. & Tan, Z. M. On the sensitivity of the relationship between Hadley circulation asymmetry and ENSO in CMIP5 models. *Geophys. Res. Lett.* 45, 9253–9259 (2018).
- Feng, J., Li, J. P., Jin, F. F., Liu, Z. Y. & Zhao, S. Effect of El Niño on the response ratio of Hadley circulation to different SST meridional structures. Clim. Dyn. 53, 3877–3891 (2019).
- Sun, Y. & Zhou, T. J. How does El Niño affect the interannual variability of the boreal summer Hadley circulation? J. Clim. 27, 2622–2642 (2014).
- Ma, J. & Li, J. P. The principal modes of variability of the boreal winter Hadley cell. *Geophys. Res. Lett.* 35, https://doi.org/10.1029/ 2007GL031883 (2008).
- Huang, R., Chen, S., Chen, W., Hu, P. & Yu, B. Recent strengthening of the regional Hadley circulation over the western Pacific during boreal spring. Adv. Atmos. Sci. 36, 1251–1264 (2019).
- Li, Y. et al. Regional perspective of Hadley circulation and its uncertainties among different datasets: spread in reanalysis datasets.
 J. Geophys. Res. Atmos. 127, https://doi.org/10.1029/ 2022JD036940 (2022).
- Huang, R., Chen, S., Chen, W. & Hu, P. Interannual variability of regional Hadley circulation intensity over western Pacific during boreal winter and its climatic impact over Asia-Australia region. *J. Geophys. Res. Atmos.* 123, 344–366 (2018).
- Ambrizzi, T., de Souza, E. B. & Pulwarty, R. S. in *The Hadley Circulation: Present, Past and Future* (eds Henry F. D. & Bradley, R. S.) 203–235 (Springer Netherlands, 2004).
- Zhao, H. & Moore, G. W. K. Trends in the boreal summer regional Hadley and Walker circulations as expressed in precipitation records from Asia and Africa during the latter half of the 20th century. *Int. J. Climatol.* 28, 563–578 (2008).
- Chen, S., Wei, K., Chen, W. & Song, L. Regional changes in the annual mean Hadley circulation in recent decades. *JGR Atmos.* 119, 7815–7832 (2014).
- Nguyen, H. et al. Variability of the extent of the Hadley circulation in the southern hemisphere: a regional perspective. *Clim. Dyn.* 50, 129–142 (2017).
- Gao, C., Chen, M., Zhou, L., Feng, L. & Zhang, R.-H. The 2020–2021 prolonged La Niña evolution in the tropical Pacific. Sci. China Earth Sci. 65, 2248–2266 (2022).

- Xie, S.-P. & Philander, S. G. H. A coupled ocean-atmosphere model of relevance to the ITCZ in the eastern Pacific. *Tellus A* 46, 340–350 (1994)
- 42. Song, X. M., Zhang, R. H. & Rong, X. Y. Dynamic causes of ENSO decay and its asymmetry. *J. Clim.* **35**, 445–462 (2022).
- Wang, B. & Zhang, Q. Pacific–East Asian teleconnection. Part II: how the Philippine Sea anomalous anticyclone is established during El Niño development*. J. Clim. 15, 3252–3265 (2002).
- Jourdain, N. C., Lengaigne, M., Vialard, J., Izumo, T. & Gupta, A. S. Further insights on the influence of the indian ocean dipole on the following year's ENSO from observations and CMIP5 models. *J. Clim.* 29, 637–658 (2016).
- Dong, D., Li, J., Huyan, L. & Xue, J. Atmospheric energetics over the tropical Pacific during the ENSO cycle. J. Clim. 30, 3635–3654 (2017).
- Zhang, Y. et al. Energetic connection between the South China Sea summer monsoon and Indian Ocean dipole from the perspective of perturbation potential energy. Clim. Dyn. 61, 2457–2470 (2023).
- 47. Lorenz, E. N. Available potential energy and the maintenance of the general circulation. *Tellus* **7**, 157–167 (1955).
- Oort, A. H. & Rasmusson, E. M. On the annual variation of the monthly mean meridional circulation. *Mon. Weather Rev.* 98, 423–442 (1970).
- Dima, I. M. & Wallace, J. M. On the seasonality of the Hadley Cell. J. Atmos. Sci. 60, 1522–1527 (2003).
- Yun, K.-S., Timmermann, A. & Stuecker, M. F. Synchronized spatial shifts of Hadley and Walker circulations. *Earth Syst. Dyn.* 12, 121–132 (2021).
- Gill, A. E. Some simple solutions for heat-induced tropical circulation.
 Q. J. R. Meteorol. Soc. 106, 447–462 (1980).
- An, S.-I. Atmospheric responses of Gill-type and Lindzen-Nigam models to global warming. J. Clim. 24, 6165–6173 (2011).
- Li, Y. et al. Interannual variability of regional Hadley circulation and El Niño interaction. *Geophys. Res. Lett.* 50, https://doi.org/10.1029/ 2022GL102016 (2023).
- Sun, Y. et al. Regional meridional cells governing the interannual variability of the Hadley circulation in boreal winter. *Clim. Dyn.* 52, 831–853 (2018).
- 55. Jin, F. F. An equatorial Ocean recharge paradigm for ENSO. Part I: conceptual model. *J. Atmos. Sci.* **54**, 811–829 (1997).
- Liu, Y. et al. Land-atmosphere-ocean coupling associated with the Tibetan Plateau and its climate impacts. *Natl. Sci. Rev.* 7, 534–552 (2020).
- Deser, C., Guo, R. & Lehner, F. The relative contributions of tropical Pacific sea surface temperatures and atmospheric internal variability to the recent global warming hiatus. *Geophys. Res. Lett.* 44, 7945–7954 (2017).
- 58. Feng, S. & Fu, Q. Expansion of global drylands under a warming climate. *Atmos. Chem. Phys.* **13**, 10081–10094 (2013).
- Post, D. A. et al. Decrease in southeastern Australian water availability linked to ongoing Hadley cell expansion. *Earth's Future* 2, 231–238 (2014)
- Schneider, U. et al. GPCC's new land surface precipitation climatology based on quality-controlled in situ data and its role in quantifying the global water cycle. *Theor. Appl. Climatol.* 115, 15–40 (2013).
- Wang, Y., Feng, J., Li, J., An, R. & Wang, L. Variability of boreal spring Hadley circulation over the Asian monsoon domain and its relationship with tropical SST. *Clim. Dyn.* 54, 1655–1669 (2019).
- Zhou, T., Yu, R., Li, H. & Wang, B. Ocean forcing to changes in global monsoon precipitation over the recent half-century. *J. Clim.* 21, 3833–3852 (2008).
- Piao, J. et al. The intensified impact of El Niño on late-summer precipitation over East Asia since the early 1990s. *Clim. Dyn.* 54, 4793–4809 (2020).
- Chen, L. & Li, G. Asymmetric effect of ENSO in the decaying stage on the central China July precipitation. Clim. Dyn. 61, 3029–3045 (2023).

- Chen, W., Wang, L. & Feng, J. How does the East Asian summer monsoon behave in the decaying phase of El Niño during different PDO phases? J. Clim. 27, 2682–2698 (2014).
- Wang, B., Li, J. & He, Q. Variable and robust East Asian monsoon rainfall response to El Niño over the past 60 years (1957–2016). Adv. Atmos. Sci. 34, 1235–1248 (2017).
- Fasullo, J. T., Otto-Bliesner, B. L. & Stevenson, S. ENSO's changing influence on temperature, precipitation, and wildfire in a warming climate. *Geophys. Res. Lett.* 45, 9216–9225 (2018).
- Lindzen, R. S. & Nigam, S. On the role of sea surface temperature gradients in forcing low-level winds and convergence in the tropics. *J. Atmos. Sci.* 44, 2418–2436 (1987).
- Kanno, Y. & Iwasaki, T. Future changes of atmospheric energy cycle in CMIP5 climate models. J. Geophys. Res. Atmos. 127, https://doi.org/ 10.1029/2021jd036380 (2022).
- Zhang, Y., Li, J., Wang, Q. & Xue, J. Variations in atmospheric perturbation potential energy associated with the South China Sea summer monsoon. *Clim. Dyn.* 53, 2295–2308 (2019).
- Zhang, B., Song, S., Wang, H., Guo, T. & Ding, Y. Evaluation of the performance of CMIP6 models in simulating extreme precipitation and its projected changes in global climate regions. *Nat. Hazards* 121, 1737–1763 (2024).
- Li, Z., Liu, T., Huang, Y., Peng, J. & Ling, Y. Evaluation of the CMIP6 precipitation simulations over global land. *Earth's Future* 10, https://doi.org/10.1029/2021ef002500 (2022).
- Guo, Y. P., Li, J. P. & Feng, J. Climatology and interannual variability of the annual mean Hadley circulation in CMIP5 models. *Adv. Clim. Change Res.* 7, 35–45 (2016).
- Li, Y., Du, M. Y., Feng, J., Xu, F. L. & Song, W. J. Relationships between the Hadley circulation and tropical sea surface temperature with different meridional structures simulated in CMIP6 models. *Front. Mar. Sci.* 10, https://doi.org/10.3389/fmars.2023.1145509 (2023).
- Cai, W. et al. ENSO and greenhouse warming. Nat. Clim. Change 5, 849–859 (2015).
- Kalnay, E. et al. The NCEP/NCAR 40-Year Reanalysis Project. Bull. Am. Meteorol. Soc. 77, 437–471 (1996).
- Hersbach, H. et al. The ERA5 global reanalysis. Q. J. R. Meteorol. Soc. 146, 1999–2049 (2020).
- Kobayashi, S. et al. The JRA-55 reanalysis: general specifications and basic characteristics. J. Meteorol. Soc. Jpn. Ser. II 93, 5–48 (2015).
- Compo, G. P. et al. The twentieth century reanalysis project. Q. J. R. Meteorol. Soc. 137, 1–28 (2011).
- Adler, R. et al. The Global Precipitation Climatology Project (GPCP) monthly analysis (New Version 2.3) and a review of 2017 global precipitation. *Atmosphere* 9, https://doi.org/10.3390/atmos9040138 (2018).
- Huang, B. et al. Extended reconstructed sea surface temperature, version 5 (ERSSTv5): upgrades, validations, and intercomparisons. *J. Clim.* 30, 8179–8205 (2017).
- Feng, J. et al. Contrasting responses of the Hadley circulation to equatorially asymmetric and symmetric meridional sea surface temperature structures. *J. Clim.* 29, 8949–8963 (2016).
- 83. Zhang, G. & Wang, Z. Interannual variability of tropical cyclone activity and regional Hadley circulation over the Northeastern Pacific. *Geophys. Res. Lett.* **42**, 2473–2481 (2015).

- 84. Chemke, R. Large hemispheric differences in the Hadley cell strength variability due to ocean coupling. *npj Clim. Atmos. Sci.* **5**, https://doi.org/10.1038/s41612-021-00225-3 (2022).
- 85. Pikovnik, M., Zaplotnik, Ž, Boljka, L. & Žagar, N. Metrics of the Hadley circulation strength and associated circulation trends. *Weather Clim. Dyn.* **3**, 625–644 (2022).

Acknowledgements

This work was supported by the National Natural Science Foundation of China (42222501), the National Key R&D Program of China (2023YFC3107702, 2022YFC3105102), the Project of Southern Marine Science and Engineering Guangdong Laboratory (Zhuhai) under contract No. SML2024SP023.

Author contributions

J.F. and J.P.L. designed the original ideas of the study. X.L.J. performed the data analysis and wrote the original manuscript, in discussion with J.F. and J.P.L. Y.Z.Z. conducted the energy related program. J.F. structured the paper. All authors contributed to the interpretation of the results and improvement of the manuscript.

Competing interests

The authors declare no competing interests.

Additional information

Supplementary information The online version contains supplementary material available at https://doi.org/10.1038/s41612-025-01221-7.

Correspondence and requests for materials should be addressed to Juan Feng.

Reprints and permissions information is available at http://www.nature.com/reprints

Publisher's note Springer Nature remains neutral with regard to jurisdictional claims in published maps and institutional affiliations.

Open Access This article is licensed under a Creative Commons Attribution-NonCommercial-NoDerivatives 4.0 International License, which permits any non-commercial use, sharing, distribution and reproduction in any medium or format, as long as you give appropriate credit to the original author(s) and the source, provide a link to the Creative Commons licence, and indicate if you modified the licensed material. You do not have permission under this licence to share adapted material derived from this article or parts of it. The images or other third party material in this article are included in the article's Creative Commons licence, unless indicated otherwise in a credit line to the material. If material is not included in the article's Creative Commons licence and your intended use is not permitted by statutory regulation or exceeds the permitted use, you will need to obtain permission directly from the copyright holder. To view a copy of this licence, visit https://creativecommons.org/licenses/by-nc-nd/4.0/.

© The Author(s) 2025